Hyperfine Interactions **130:** 81–108, 2000.

Grain boundaries of nanocrystalline materials – their widths, compositions, and internal structures

B. Fultz and H.N. Frase

California Institute of Technology, mail 138-78, Pasadena, CA 91125, USA

Nanocrystalline materials contain many atoms at and near grain boundaries. Sufficient numbers of Mössbauer probe atoms can be situated in grain boundary environments to make a clear contribution to the measured Mössbauer spectrum. Three types of measurements on nanocrystalline materials are reported here, all using Mössbauer spectrometry in conjunction with X-ray diffractometry, transmission electron microscopy, or small angle neutron scattering. By measuring the fraction of atoms contributing to the grain boundary component in a Mössbauer spectrum, and by knowing the grain size of the material, it is possible to deduce the average width of grain boundaries in metallic alloys. It is found that these widths are approximately 0.5 nm for fcc alloys and slightly larger than 1.0 nm for bcc alloys.

Chemical segregation to grain boundaries can be measured by Mössbauer spectrometry, especially in conjunction with small angle neutron scattering. Such measurements on Fe–Cu and Fe_3Si–Nb were used to study how nanocrystalline materials could be stabilized against grain growth by the segregation of Cu and Nb to grain boundaries. The segregation of Cu to grain boundaries did not stabilize the Fe–Cu alloys against grain growth, since the grain boundaries were found to widen and accept more Cu atoms during annealing. The Nb additions to Fe_3Si did suppress grain growth, perhaps because of the low mobility of Nb atoms, but also perhaps because Nb atoms altered the chemical ordering in the alloy.

The internal structure of grain boundaries in nanocrystalline materials prepared by high-energy ball milling is found to be unstable against internal relaxations at low temperatures. The Mössbauer spectra of the nanocrystalline samples showed changes in the hyperfine fields attributable to movements of grain boundary atoms. In conjunction with SANS measurements, the changes in grain boundary structure induced by cryogenic exposure and annealing at low temperature were found to be somewhat different. Both were consistent with a sharper density gradient between the crystalline region and the grain boundary region.

1. Introduction

A high density of grain boundaries is one reason why nanocrystalline materials have unconventional properties [1–3]. The atomic structures of grain boundaries in nanocrystalline materials have been controversial. Early reports of a highly disordered, "gas-like" structure at grain boundaries [1–5] were not confirmed by other diffraction studies [6–9] or by high resolution transmission electron microscopy (HREM) studies of fcc materials [10–14]. It has proved difficult to make quantitative measurements on subnanometer structural features, especially when these features are arranged irregularly in a material. Grain boundaries imaged in HREM, for example, tend to be those with

special orientation relationships between the crystallites, and may not be typical of all grain boundaries. X-ray powder diffraction experiments can, in principle, determine the average atomic structure of grain boundaries, but this requires a difficult and usually ambiguous separation of the diffractions from grain boundaries and the diffractions from crystallites. Large static disorder has been observed in extended X-ray absorption fine structure (EXAFS) measurements on nanophase materials [15], but again it is difficult to separate the effects of grain boundaries from the effects of crystallites.

Mössbauer spectrometry has become an important experimental technique for the characterization of nanocrystalline materials. The hyperfine fields measured by Mössbauer spectrometry are perturbed by the local structural disorder at grain boundaries. The spectral components from these distorted local environments are superimposed on a spectrum from atoms in regular crystalline sites, however, so the signals from grain boundary environments are too weak to identify in Mössbauer spectra from most bulk materials. For nanocrystalline materials, however, the high fraction of atoms at grain boundaries has made Mössbauer spectrometry a practical technique for detailed studies of grain boundaries. Earlier studies of nanocrystalline materials demonstrated the capabilities of Mössbauer spectrometry for phase analysis and for identification of spectral components from grain boundaries [16–24]. Mössbauer spectrometry is now commonplace for investigations on Fe-containing nanocrystalline materials, and ^{119}Sn Mössbauer spectrometry has even become important for studies of nanocrystalline Sn in electrode materials for rechargeable batteries [25,26]. So many results have now been reported on ^{57}Fe Mössbauer spectrometry studies on nanocrystalline materials prepared by mechanical attrition that this subtopic has been the subject of an extensive review by Campbell and Kaczmarek [27]. The present paper serves to review and extend a number of results from our group on Mössbauer spectrometry studies on grain boundaries of nanocrystalline materials prepared by high energy ball milling.

Geometrical arguments suggest that with 10 nm crystallites and a grain boundary width of 1 nm, about one-quarter of all atoms should be within grain boundaries. A more precise determination of this fraction, and a determination of the widths of grain boundaries in nanocrystalline metals, is the subject of one of the investigations described here. For several fcc and bcc Fe alloys, we were able to quantify the fraction of ^{57}Fe atoms that contributed to the grain boundary component of a Mössbauer spectrum [28]. The grain size was determined independently by X-ray diffractometry and dark-field transmission electron microscopy (TEM). These grain size data were used in a microstructural model to determine the surface area of grain boundaries. The average width of the grain boundary was the parameter that provided consistency between the Mössbauer grain boundary fraction and the grain boundary area. This was 0.5 nm for fcc alloys, and a bit larger than 1 nm for bcc alloys.

Polycrystalline materials are generally unstable against grain growth. Nanocrystalline materials are especially unstable, owing to their large grain boundary area. Nanocrystalline materials may even be far from thermodynamic equilibrium, since their enthalpies of grain growth are a few kJ/mol [29–32], which are at least comparable to thermal energies, $k_{\mathrm{B}}T$, at modest temperature. Since many of the interesting properties

of nanocrystalline materials derive from their small crystallite size, it is important to consider strategies to stabilize them against grain growth. Consolidation of powdered materials with the application of heat and pressure usually promotes grain growth, and sometimes the loss of the desired properties. Nanocrystalline materials are expected to be unstable thermodynamically against grain growth, because grain growth will minimize the energy cost of grain boundary formation, E_{form}. On the other hand, a positive entropy of grain boundary formation, S_{form}, will compensate somewhat this energy, and therefore enhance the thermodynamic stability of nanocrystalline materials at finite temperatures. At modest temperatures of 500 K or so, however, it seems that the contribution $-T\,S_{\text{form}}$ to the free energy is too small to offset E_{form} to actually stabilize a nanocrystalline material against grain growth. Evidence for the smallness of $-T\,S_{\text{form}}$ can be obtained by considering the entropy of fusion of a solid,[1] and the increased vibrational entropy of the nanocrystalline materials also seems too small to offset the energy penalty of grain boundary formation [33,34].

A method for stabilizing nanocrystalline materials against grain growth by control of alloy chemistry was discussed by Johnson and Abe [35], and later Weissmüller [36]. It involves the suppression of grain growth by obtaining microstructures that have a strong grain boundary segregation of one of the solute species. The growth of grains, and the loss of grain boundary area, might require the energetically unfavorable redissolution of the solute within the crystallites. The Mössbauer spectrometry experiments reported in this paper indicate that this thermodynamic argument need not be valid because the width of the grain boundary may change to accommodate more solute. On the other hand, a segregant with low diffusivity may suppress grain growth by a "solute drag" mechanism [37].

Although grain boundaries in nanocrystals have similarities to conventional grain boundaries in large-grained materials, some differences have been suggested by previous work, and changes within grain boundaries could occur upon annealing [8,38–40]. Considering the large volume fraction of grain boundaries in nanocrystalline materials, differences in the local atomic structure of grain boundaries could affect macroscopic properties such as mechanical deformation and atomic diffusivities [41–43]. Different methods of synthesis may produce different types of grain boundaries in nanocrystalline materials. Nanocrystals prepared by mechanical attrition may have grain boundaries inherently different from grain boundaries in gas-condensed nanocrystals. There is some evidence that mechanical attrition creates grain boundaries having a higher energy than equilibrated high-angle grain boundaries [44]. We expected it may be possible to induce atomic rearrangements within grain boundaries by low temperature thermal treatments that have no effect on grain growth. We report results from Mössbauer and small angle neutron scattering (SANS) measurements that show changes in the atomic density of the grain boundaries when nanocrystalline Ni_3Fe is exposed to cryogenic temperatures, or annealed at 100°C. Annealing at 265°C served to cause a change in grain boundary

[1] Assuming similar structures for grain boundaries and liquids, the entropy of fusion will not stabilize the structure until the melting temperature is reached.

density, and a large change in the magnetic moments of the atoms in the grain boundaries.

This paper reports three investigations on the atomic structure and composition grain boundaries in nanocrystalline metallic alloys. Section 2 describes experimental aspects common to all three studies. The first investigation, described in section 3, used Mössbauer spectrometry to show that the average widths of grain boundaries are different in fcc and bcc nanocrystals. Mössbauer spectrometry was used to measure the intensity of the "grain boundary component" in the hyperfine field distributions of nanocrystals, related to the number of ^{57}Fe atoms in grain boundaries. Other experimental techniques, X-ray diffractometry and transmission electron microscopy, were needed to obtain the crystallite size distribution. Grain boundary widths were finally determined when a Monte Carlo method was used to ensure consistency between the number of grain boundary atoms and the grain size of model and real materials. Section 2 describes approaches to the engineering of nanocrystals with improved stability against grain growth. We report results from two nanocrystalline materials, Fe_3Si with Nb additions, and Fe–Cu alloys. Both the Nb in the first alloy and the Cu in the second alloy are grain boundary segregants. The Cu segregation did not suppress grain growth, but Nb was more successful. Unfortunately, it is not obvious if it was the segregation of Nb to grain boundaries, or its effect on chemical ordering in Fe_3Si that was primarily responsible for the beneficial effect of Nb additions. Section 3 describes recent observations of atomic and magnetic changes in nanocrystalline materials that occur after mild thermal treatments that had no effect on grain growth. After these low temperature annealings or cryogenic exposure, small but reproducible changes to the Mössbauer spectra and small angle neutron scattering profiles were measured. We interpret these as atom movements from high energy to lower energy sites in the grain boundaries of nanocrystalline materials prepared by high energy ball milling.

2. Experimental

We prepared nanocrystalline alloys by mechanical attrition with a SPEX 8000 laboratory mixer/mill [16,19,20,28,45]. Elemental powders were mixed in appropriate amounts, for the alloys of interest. The present manuscript presents specific results on the grain boundary widths of bcc Cr–Fe, Fe–Ti, and Mo–Fe, and fcc Ni–Fe and Fe–Mn, grain growth in Fe–Cu and Fe_3Si–Nb, and grain boundary relaxations in fcc Ni–Fe. Our earlier powders were sealed in a tungsten carbide vial with tungsten carbide balls under an argon atmosphere. In later work we used hardened steel vials and lids, into which knife edges were machined to make metal–metal seals against a Cu gasket. This seal was shown to be leakproof to hydrogen gas during 18 h of milling. The ball-to-powder weight ratio varied from 4 : 1 to 20 : 1, and the materials were milled at room temperature with forced air cooling. The as-milled powders were annealed at various temperatures in evacuated quartz ampoules to induce grain growth, chemical segregation, ordering, or internal relaxations of the grain boundary structure.

Mössbauer spectra were measured in transmission geometry at room temperature with a conventional constant-acceleration spectrometer. Radiation sources of 5–20 mCi ^{57}Co in a Rh matrix were used. We obtained hyperfine magnetic field (HMF) distributions from the spectra using the method of Le Caër and Dubois [46], and this method was also used for obtaining correlations between the isomer shift and the HMF.

X-ray diffractometry was performed with an Inel CPS-120 diffractometer using Co Kα radiation and a curved position-sensitive detector spanning a 2θ angle of 127°. Grain sizes were determined from X-ray diffraction peak widths using a k vs. Δk extrapolation method of Williamson and Hall to extract grain size [47]. The method of Warren and Averbach [28,48–50] was also used to extract the strain and size contributions to the broadening of some X-ray peaks, using the (1 1 0) and (2 2 0) bcc diffractions, for example. Unfortunately, for bcc alloys with the largest size broadenings we were unable to adequately account for the overlap of the tails of the (2 0 0) and (1 1 0) diffraction peaks in a Warren–Averbach analysis. This led to problems in determining the backgrounds under the diffraction peaks, which affected the accuracy of the low order Fourier components. The method of Warren and Averbach was more reliable for materials with less peak broadening, giving, for example, a grain size of 8.8 nm for our bcc Fe–V alloy as opposed to the size of 7.9 nm obtained from y-intercept of the plot of Δk vs. k. More importantly, grain sizes were checked by dark-field imaging performed with a Philips EM 430 transmission electron microscope (TEM).

Transmission electron microscopy was performed with a Philips EM430 microscope operated at 300 kV. Specimens for TEM were prepared by grinding the sample powder in a mortar and pestle, and sprinkling some of the powder onto a holey carbon microscope grid. Some of the TEM dark field images were digitized, enhanced in contrast, and used for obtaining distributions of intercept lengths of random lines crossing the diffracting particles. Image processing was performed with the software package Image 1.40 running on a Macintosh II computer. Chemical microanalysis was performed by energy dispersive X-ray spectrometry (EDX) with an EDAX 9900 spectrometer mounted on the TEM.

3. Grain boundary widths

Assuming the average width of grain boundaries to be the same for materials with different grain size, a larger-grained material will have a smaller fraction of its atoms within grain boundaries than will the smaller-grained material.[2] The distorted local environments around ^{57}Fe atoms located at and near grain boundaries contribute a distinct sub-spectrum to the Mössbauer spectra of nanocrystalline materials. Atoms at the edges of the crystallites, and perhaps within crystallites near the grain boundaries, will also contribute to this grain boundary subspectrum. Obtaining the grain boundary width by comparing the fraction of the grain boundary subspectrum to the grain size may there-

[2] This assumption of a constant average width is confirmed in the course of the work by examining the trend in the grain boundary fraction for materials of different grain size.

fore overestimate the width of the grain boundary. Other uncertainties in these measurements are the chemical composition within the grain boundary (fortunately, however, the method of high energy ball milling tends to homogenize the chemical composition of the material), the atomic density of the grain boundary, and of course the experimental uncertainties of isolating the grain boundary and crystalline components of the Mössbauer spectrum. For this reason, after an initial report of the method [19], we performed measurements on several different alloy systems to test the reliability of this method for grain boundary width determinations [28], and we present some new results on Ni_3Fe in this paper. The results do not provide a detailed picture of the internal structures of grain boundaries, but the widths of grain boundaries do constrain the possible internal structures. If the average widths of grain boundaries are only a few angstroms, a high degree of disorder in the grain boundaries (such as a gas-like phase) is unreasonable. If, on the other hand, the widths of the grain boundaries are 2 nm or more, disordered atom arrangements in grain boundaries are more plausible.

We found significant differences between the individual Mössbauer spectra of nanocrystalline bcc Cr–Fe, Fe–Ti, Mo–Fe, and nanocrystalline fcc alloys Ni–Fe and Fe–Mn. Only the Ni–Fe alloys were strongly ferromagnetic (figure 1), and this allowed the cleanest separation of the grain boundary component. The separation of spectral components was facilitated by obtaining the distribution of hyperfine magnetic fields (HMF's) using the method of Le Caër and DuBois [46]. The prominent peak in the HMF distribution of the large-grained control sample is centered on 287 kG, typical of disordered Ni_3Fe [51–53]. We expect the HMF's of ^{57}Fe atoms in crystalline local environments to be about 287 kG. The intensity in the HMF distribution below 242 kG has been shown[3]

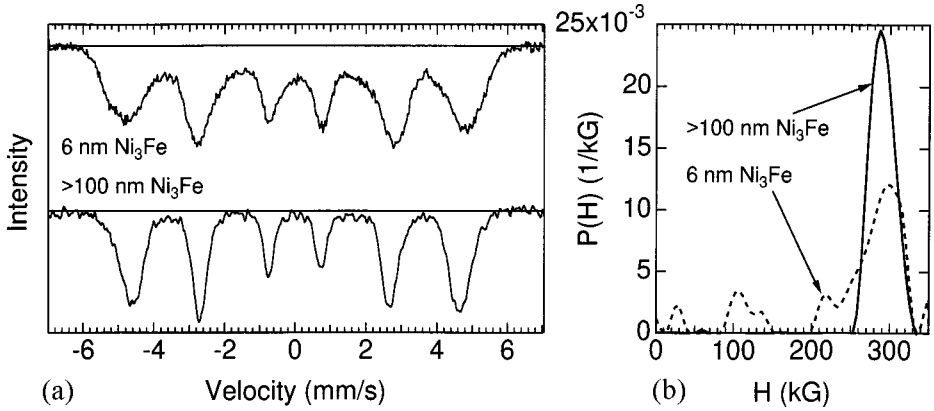

Figure 1. (a) Mössbauer spectra from nanocrystalline fcc Ni_3Fe milled for 24 h with a ball-powder weight ratio of 20 : 1. This material had an average grain size of 6 nm. Also shown is a spectrum from a control sample obtained by annealing nanocrystalline powder for 1 h at 800°C. (b) Hyperfine magnetic field distributions of the spectra of part (a). Grain boundary component is from 0–242 kG.

[3] This assignment is supported by comparing the spectral areas for samples of different grain sizes, as will be shown later in figure 3.

to originate with ^{57}Fe atoms in and adjacent to, grain boundaries [28,54]. This low field component of the HMF distribution from the nanocrystalline material accounts the broad component in the Mössbauer spectrum beneath the main sextet from crystalline Ni_3Fe. The detailed structure of this part of the HMF distribution is not unique, and the peaks in this range of HMF can be altered by different choices of fitting parameters such as instrument linewidth. The areas are reliable, however, as are the first moments.

It is also known that the spectra of Fe–Mn alloys are broadened by a small hyperfine magnetic field [55]. There was a reduction in the breadth of the spectrum of bcc Cr–Fe when the sample was in an applied magnetic field [19], consistent with a hyperfine magnetic field of opposite sign from the lattice magnetization. Mössbauer spectra of the three alloys fcc Ni–Fe, fcc Fe–Mn, and bcc Cr–Fe were therefore analyzed to obtain HMF distributions. Mössbauer spectra from the alloys bcc Mo–Fe and Fe–Ti were analyzed both with a distribution of hyperfine magnetic fields, and a distribution of electric field gradients. Although we are unsure which distribution is physically meaningful, both analyses fortunately gave similar results for the fractional area of the grain boundary component in the spectrum. Although most Mössbauer spectra were acquired at room temperature, measurements on Cr–Fe, Mo–Fe, and Ni–Fe were also performed at 4 K to confirm that the spectral broadening was not caused primarily by a magnetic relaxation phenomenon such as superparamagnetism.

The second measurements required for the determination of grain boundary widths were the grain sizes of the nanocrystalline alloys. These were determined by X-ray lineshape analysis in conjunction with TEM dark-field analysis. Most of the X-ray lineshape analyses employed the Δk vs. k extrapolation method of Williamson and Hall [47]. We found it useful to employ dark-field imaging in a TEM for more definitive grain size determinations. Figure 2(b) presents a TEM dark-field image, and figure 2(c) of how the particle size distribution was extracted from it. For comparison, an X-ray diffraction lineshape, broadened largely by particle size effects, is shown in figure 2(a).

The third task for determining grain boundary widths was to construct a geometrical relationship between the grain boundary volume fraction determined by Mössbauer spectrometry and the grain size determined by X-ray diffractometry and TEM. This can be approximated by examining the surface areas of some simple geometrical objects, but our most reliable estimate of grain boundary volume fraction came from a Monte Carlo simulation of a polycrystalline microstructure [28,54]. The simulation used an algorithm where seeds distributed at random on a lattice were used to nucleate crystals that grew to impingement. It was straightforward to vary the grain size by controlling the seed density. It was also straightforward to determine the column length distribution by passing lines through the microstructure and sorting the line segments across each grain. The column length distribution was in reasonable agreement with the column length distribution deduced from the TEM dark field images. Counting the grain boundary atoms required an unconventional algorithm, however. Lattice sites were assigned to “crystals” or “grain boundaries” on the basis of their nearest neighbors. For a narrow grain boundary, the algorithm would count as grain boundary atoms only those sites with one or more first-nearest-neighbors (1nn) in a different crystal. A thicker grain

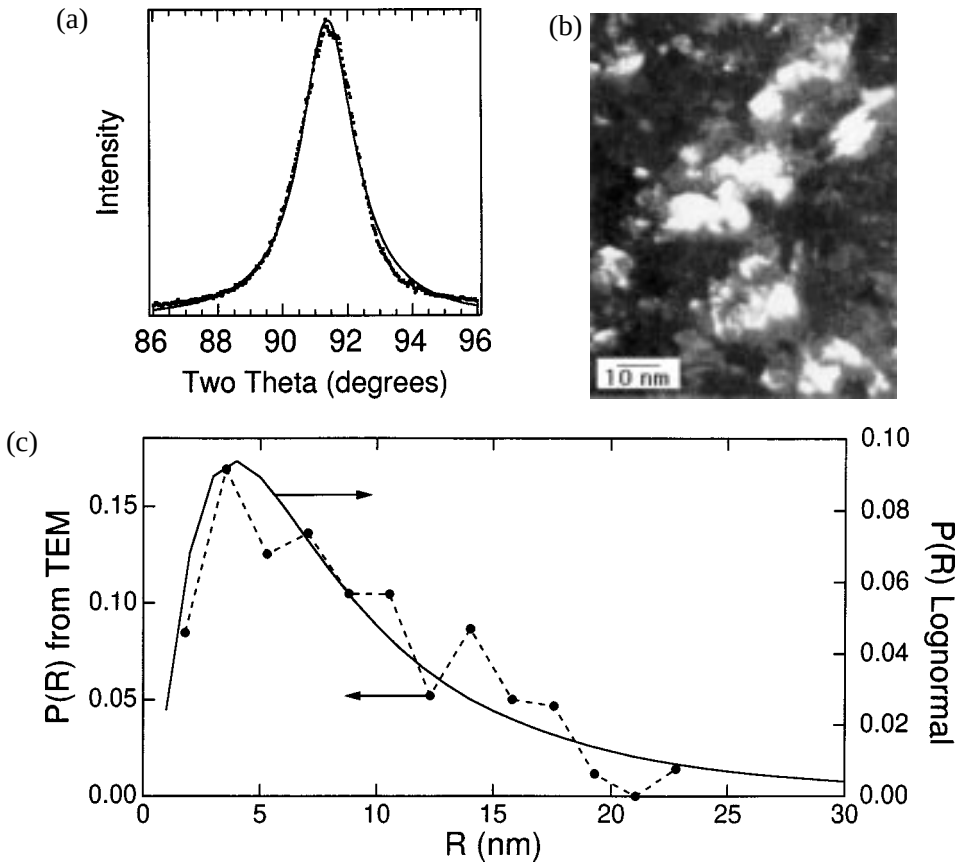

Figure 2. (a) (2 2 0) X-ray diffraction peak from nanocrystalline fcc Ni_3Fe of 15 nm grain size. (b) (1 1 1) TEM dark-field image of the same powder. (c) Probability distribution of the volume fraction of spherical grains of radius R in increment ΔR, $P(R)\Delta R$, extracted from the image of part (b) by the use of the equation:

$$\rho(l) \propto \sum_{2R=l}^{\infty} \frac{1}{\sqrt{(2R/l)^2 - 1}} P'(R)\Delta R,$$

where $\rho(l)$ is the distribution of intercept lengths in the 2-dimensional image of part (b), and $P'(R)\Delta R$ is the fractional amount of area occupied by spherical particles of radius from R and $R + \Delta R$. The volume fraction, $P(R)\Delta R$, is proportional to $P'(R)R\Delta R$.

boundary would count, for example, any atom with a third-nearest-neighbor (3nn) atom in a different crystal. By using approximate lattice parameters of the bcc and fcc Fe alloys, the grain boundary component could be determined as a function of the grain size obtained from X-ray lineshape analysis. Two such calculated curves are presented in figure 3 as solid lines. We see that the "9nn" model provides the most accurate grain boundary fraction for the bcc alloys, and the "3nn" model works best for the fcc alloys. Finally, to obtain an actual width of the grain boundary, it was necessary to convert the

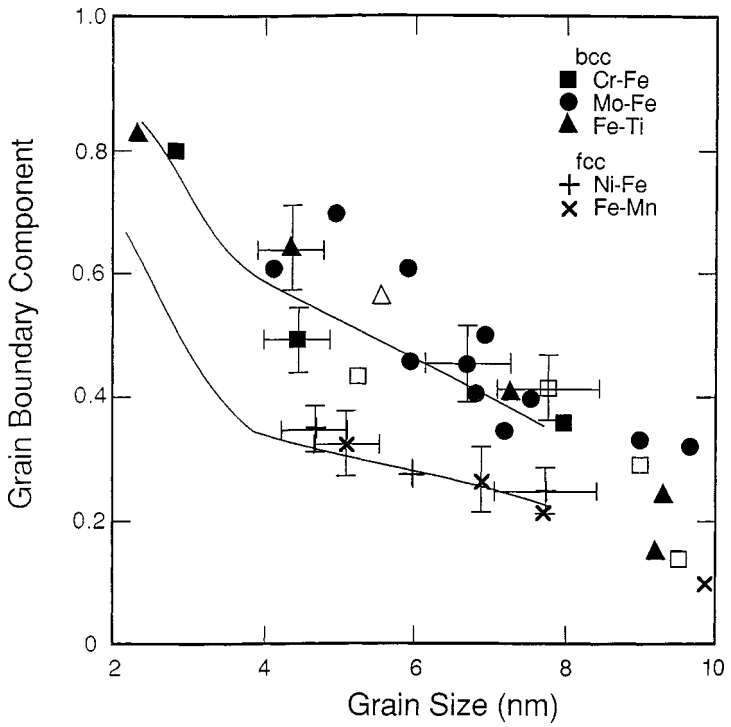

Figure 3. Fractional amount of grain boundary HMF component versus grain size. Solid symbols: material after ball milling for various times. Open symbols: material milled for 96 h, after annealing at 300°C for various times. Crosses: fcc alloys (Fe–Mn data as-milled, Ni–Fe datum at 7.5 nm obtained after annealing). Solid curves are results from Monte Carlo simulations "9nn" top, and "3nn" bottom, described in the text.

width in terms of the nearest-neighbor algorithm to a physical width. The length of the jth nearest-neighbor distance is too large for a structural width of the grain boundary, since it also includes atoms at the edges of crystallites as part of the grain boundary fraction. Approximately, the structural width of the grain boundary was taken as the jth nearest-neighbor distance minus a thickness of two unit cell edge lengths.

The experimental data of figure 3 show a difference between the grain boundaries of fcc and bcc metals. We obtain a structural width of the boundary of about 1.2 nm for the bcc alloys Cr–Fe and Fe–Ti, perhaps slightly larger for bcc Mo–Fe, and about 0.5 nm for the fcc alloys Ni–Fe and Fe–Mn. The grain boundary widths for the fcc alloys are in reasonable agreement with the results of HREM observations of grain boundary widths in fcc metals such as Al, Au, Pd, Pb, and Cu [10–14]. Few HREM observations of grain boundaries in bcc metals have been reported (especially ferromagnetic Fe alloys), except for symmetric tilt boundaries in large crystals [56,57].

Clearly it is unreasonable to attribute a "gas-like" arrangements of atoms in grain boundaries of 0.5 nm in average width. There is simply not enough volume around a grain boundary atom to allow for the wide distribution of interatomic separations in a gas structure. The grain boundaries in fcc nanocrystals do not seem qualitatively dif-

ferent from grain boundaries in fcc alloys of larger grain size. The grain boundaries in the nanocrystalline bcc alloys seem somewhat more disordered, with a characteristic width of about 1 nm. It is still probably unreasonable to attribute a "gas-like" atom arrangements to bcc grain boundaries, since such a gas would be confined to a width of 1 nm. There is also the possibility that the widths of the bcc grain boundaries may be slightly overestimated. The measurements described here are more properly described as a "magnetic width" of the grain boundary, and may reflect disturbances in the HMF's at ^{57}Fe atoms near the edges of the crystallites.

4. Grain boundary chemical segregation

The segregation of solute atoms to grain boundaries may help stabilize nanocrystalline materials against grain growth. In many alloy systems having positive heats of mixing, the minority species undergo a chemical segregation to grain boundaries. This chemical segregation can be quite large; chemical enrichments of the solute concentration at grain boundaries with respect to the bulk can be factors of 1,000 or more. Given a fixed number of sites in the grain boundaries and in the crystalline interiors, it is possible to calculate the difference in free energy between an alloy with solute in the crystallites and the alloy with solute on grain boundaries. This can be 10–100 kJ per mole of solute. With large fractions of atoms at grain boundaries, this contribution to the free energy can be significant for the bulk thermodynamics of nanophase materials. By saturating the grain boundary sites with solute atoms that are unfavorably dissolved in the bulk, perhaps grain growth could be suppressed. Grain growth would reduce the number of grain boundary sites available to solute atoms, perhaps sending the solute atoms back into solution in the crystallites. This thermodynamic argument depends on the existence of a fixed number of grain boundary sites, however, and will not succeed if the grain boundary is free to thicken, for example. There are also kinetic mechanisms whereby solute segregation to grain boundaries could suppress grain growth. The migration of a grain boundary during grain growth may require the segregated solute atoms to undergo diffusion to follow the boundary motion. Low diffusive mobilities of the segregants could therefore suppress grain growth.

This section describes two experimental tests of how grain boundary segregation affects grain growth. In the first experiment the segregant was Nb in Fe_3Si, and in the second the segregant was Cu in bcc Fe. As the minority species (Nb and Cu) segregated to grain boundaries during low temperature annealings, distinct changes were seen in the ^{57}Fe isomer shift distribution (for Nb segregation) and in the ^{57}Fe HMF distribution (for Cu segregation). These Mössbauer spectroscopic data on chemical segregation were correlated to the grain growth during low temperature annealings.

4.1. Nb segregation in $(Fe_3Si)_{0.95}Nb_{0.05}$

The solubility of Nb in bcc Fe is limited to about 1 at.% at low temperatures [58]. By the Hume–Rothery 15% size rule, we also expect the solubility of Nb to be low in

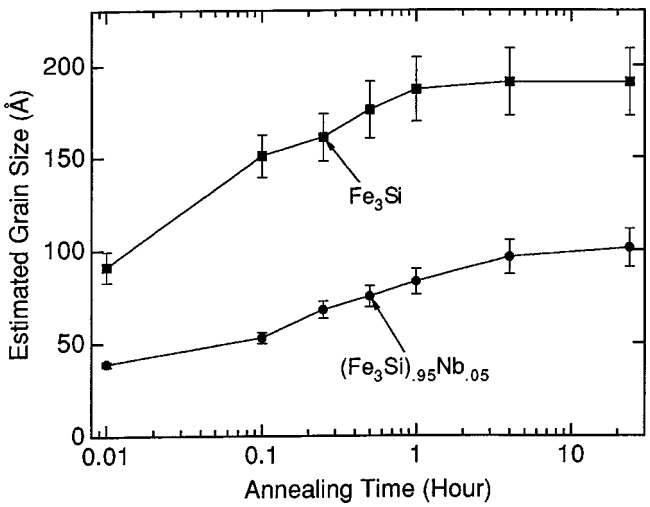

Figure 4. Grain growth in Fe_3Si and in $(Fe_3Si)_{0.95}Nb_{0.05}$ at 450°C.

Fe_3Si, owing to the much larger metallic radius of Nb (1.43 Å) than Fe (1.24 Å) or Si (1.17 Å) [59]. Figure 4 shows the effect of a 5% Nb addition on grain growth in Fe_3Si [60,61]. The ternary $(Fe_3Si)_{0.95}Nb_{0.05}$ alloy has a greater stability against grain growth than the binary Fe_3Si alloy.[4] For example, after 24 hours of annealing at 450°C, the grain size for the ternary alloy was about 10 nm, while that of the binary alloy was about 20 nm. These grain sizes were further confirmed by TEM dark-field imaging which showed that the grains of the ternary $(Fe_3Si)_{0.95}Nb_{0.05}$ alloy were mostly less than 10 nm after 24 hours annealing at 450°C.

The alloy $(Fe_3Si)_{0.95}Nb_{0.05}$ is a convenient alloy for the study of local chemistry and state of chemical order by Mössbauer spectrometry. The Mössbauer spectra (e.g., figure 5) provided a detailed picture of the first-nearest-neighbor shell of atoms around ^{57}Fe atoms, although this picture is averaged over all ^{57}Fe atoms in the specimen. The ^{57}Fe hyperfine magnetic field (HMF) distributions and isomer shifts from as-milled and annealed alloys of $(Fe_3Si)_{0.95}Nb_{0.05}$ are presented in figure 6. For the HMF distribution, the most prominent features are the two peaks at about 197 kG and 313 kG that grow during annealing. These two peaks originate from the two different sites for Fe atoms in the $D0_3$ ordered structure [62]. The peak at 313 kG is from ^{57}Fe atoms with zero Si atoms as first-nearest-neighbors (1nn), and the peak at 197 kG is from ^{57}Fe atoms with four Si atoms as first-nearest-neighbors. In a well-annealed specimen, these two peaks have intensities approximately in the ratio of 2 : 1, which is the proportion of these two sites in the $D0_3$ structure. In the binary Fe_3Si alloy the two main peaks start to develop at 197 kG and 313 kG. In the ternary $(Fe_3Si)_{0.95}Nb_{0.05}$ alloy annealed for 30 minutes, however, these two peaks are initially shifted downwards by about 10 kG (figure 6(a)).

[4] Although both alloys doubled their grain size during the annealings, grain growth is driven by curvature, which is larger in the smaller-grained $(Fe_3Si)_{0.95}Nb_{0.05}$ alloy.

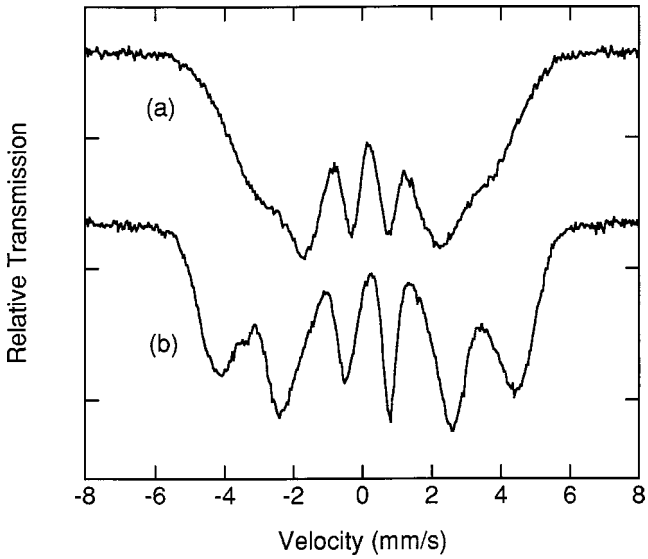

Figure 5. Mössbauer spectra of as-milled powder: (a) $(Fe_3Si)_{0.95}Nb_{0.05}$ and (b) Fe_3Si.

The subsequent upwards shift in HMF of the peaks at 197 kG and 313 kG is not found for the binary Fe_3Si alloy. This shift is attributable to a loss of Nb atoms from the nearest neighbor shells of ^{57}Fe atoms during annealing.

Niobium was also responsible for a difference in the isomer shifts (IS) of the as-milled alloys of Fe_3Si and $(Fe_3Si)_{0.95}Nb_{0.05}$. Although the primary hyperfine perturbation is magnetic, effects of the isomer shifts are seen in the symmetry of the two spectra shown in figure 5. The top spectrum from $(Fe_3Si)_{0.95}Nb_{0.05}$ has reflection symmetry about its center, whereas the bottom spectrum from Fe_3Si does not. The peaks on the positive Doppler velocity side of the spectrum from Fe_3Si are narrower than those on the negative side. The isomer shifts are more positive for ^{57}Fe atoms having smaller hyperfine magnetic fields, so the sextets with smaller separations are shifted further to the right in the figure. The peaks at positive velocity are narrower because this rightward isomer shift tends to counteract the leftward shifts associated with smaller HMF's.

The relation between the sextet offsets (the isomer shift, IS), and the sextet splittings (the hyperfine magnetic field, HMF) was assumed to be linear:

$$\mathrm{IS} = A \times \mathrm{HMF} + B. \tag{1}$$

The coefficients, A and B, were determined by the best fit of the simulated spectra to the experimental spectra. The as-milled ternary alloy had essentially the same IS for all chemical environments (giving a much more symmetrical spectrum than for the binary alloy [61,63]). The IS versus HMF for the same alloys are presented in figure 6(b). Large changes in the IS occur during the first hour of annealing at 450°C, coinciding with the 10 kG upwards shift of the main peaks in the HMF distribution. On the other hand, the IS for the binary alloy of Fe_3Si did not change during annealing, and the

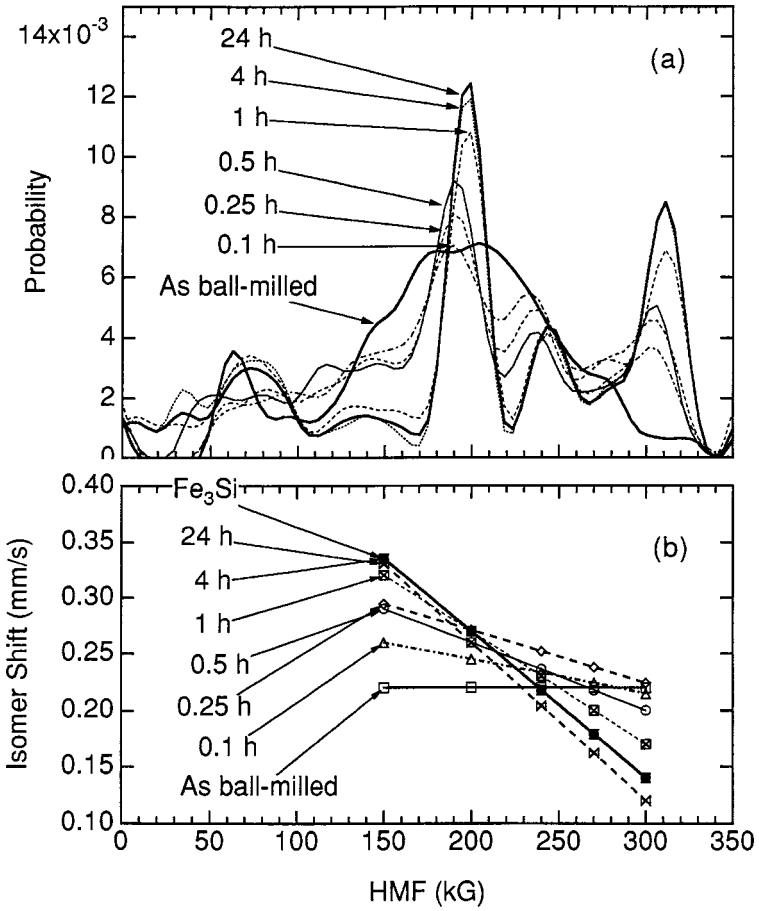

Figure 6. (a) HMF distribution for the $(Fe_3Si)_{0.95}Nb_{0.05}$ alloys as-milled and after annealing at 450°C for various times. (b) Isomer shift versus HMF for the same alloys.

relationship between IS and HMF for this binary alloy is also indicated in figure 6(b). Notice that after 4 hours of annealing, the IS for the ternary alloy of $(Fe_3Si)_{0.95}Nb_{0.05}$ became identical to the IS of the binary alloy of Fe_3Si. We attribute this change in IS of the ternary alloy to a depletion of Nb atoms as nearest neighbors of ^{57}Fe atoms.

We can use the IS distribution of figure 6(b), or equivalently the slope, A, of equation (1), as an experimental indicator of when Nb is present in the Fe_3Si crystallites, and when it is not. The IS distribution changed rapidly during the first hour of annealing at 450°C, and became identical to that of the binary Fe_3Si alloy after 4 hours of annealing. The IS distribution in the annealed alloy shows that Nb leaves the ordered Fe–Si domains, consistent with our interpretation of the changes in the HMF distribution. Unfortunately, Mössbauer spectrometry cannot distinguish between the segregation of Nb atoms to grain boundaries and the segregation of Nb atoms to zones within the bcc Fe_3Si crystallites. It is difficult to imagine, however, how the formation of Nb-rich zones could

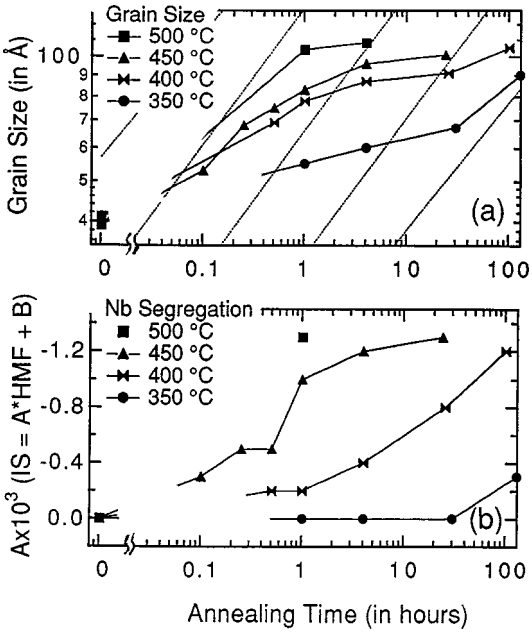

Figure 7. (a) Grain growth of $(Fe_3Si)_{0.95}Nb_{0.05}$ at various temperatures. (b) Nb segregation in $(Fe_3Si)_{0.95}Nb_{0.05}$ at various temperatures from the slope, A, in eq. (1).

suppress grain growth. We therefore attribute the loss of Nb atoms from the vicinity of Fe atoms as a segregation of Nb to grain boundaries.

In figures 7(a) and (b) we compare the extent of grain growth (determined by X-ray diffractometry) and Nb segregation (determined by Mössbauer spectrometry) for $(Fe_3Si)_{0.95}Nb_{0.05}$ annealed at various temperatures. The Nb segregation is weak at low temperatures, but is stronger at higher temperatures. The grains started to grow after short annealings at the low temperature of 350°C. For normal curvature-driven grain growth, we expect a relation between grain size, d, and time, t, approximately as $d \propto t^{1/3}$. In the log–log plot of figure 7(a), such relations are drawn as straight lines. For our samples annealed at 400°C and 450°C, grain growth followed approximately this $t^{1/3}$ relationship for times up to an hour or so. This time coincides with the time required for Nb segregation. After Nb segregation has occurred, grain growth is slowed, again indicating that Nb segregation impedes grain growth in nanocrystalline $(Fe_3Si)_{0.95}Nb_{0.05}$.

We also found a correlation between the processes of chemical ordering and Nb segregation. We suggest that with the expulsion of Nb atoms from the Fe–Si matrix, $D0_3$ chemical order is better able to develop within the Fe_3Si crystallites. The three processes of grain growth, ordering, and Nb segregation may be interdependent. This clouds any possible causal relationship between Nb segregation and grain growth. There is the alternative possibility that the development of $D0_3$ chemical order may itself suppress grain growth [64].

4.2. Cu segregation in Fe–Cu

The alloy Fe–Cu has a heat of mixing that is large and positive, so it seemed a good candidate for suppression of grain growth by Cu segregation to grain boundaries. The ^{57}Fe Mössbauer spectra of all bcc Fe–Cu alloys comprise a sextet of well-resolved peaks, broadened by the effects of Cu atoms. This broadening can be used to determine the local chemical composition of the bcc phase, which will change during the chemical segregation of Cu. Unfortunately, standard samples with high Cu concentration are not possible to prepare by conventional means, since Fe–Cu alloys with more than 1% Cu are far from chemical equilibrium at room temperature. Checking the chemical composition, and especially its homogeneity, is not possible even with microbeam analysis techniques because chemical unmixing could occur on nm spatial scales. Samples for composition calibration of the Mössbauer spectra are therefore not available. It was necessary to use the systematics of hyperfine magnetic field perturbations so that Mössbauer spectrometry itself could be used for determining the composition of the nonequilibrium Fe–Cu alloys [65]. The results of this work have since been confirmed by extended X-ray absorption fine structure (EXAFS) measurements [66].

The systematics of how the ^{57}Fe hyperfine magnetic field (HMF) distribution is affected by neighboring solute atoms have been established in terms of conduction and core electron polarizations, and we calculated HMF distributions for Fe–Cu alloys [65, 67] with a method described previously [68]. The HMF at the ^{57}Fe nucleus is obtained as the sum of two components. The first component, H_{L}, is caused by the unpaired 3d electrons local to the ^{57}Fe atom. These unpaired 3d electrons polarize, through exchange interactions, all electrons in their vicinity. This includes the core polarization (CP) of the 1s, 2s, relativistic 2p, and 3s electrons, plus the conduction electron polarization (CEP) of the 4s electrons. All these electrons have wavefunctions that are nonzero at the ^{57}Fe nucleus, so their spin imbalances can contribute to the HMF. Changes in H_{L} are proportional to changes in the local magnetic moment at the ^{57}Fe atom, $\Delta\mu(0)$, induced by neighboring solute atoms:

$$\Delta H_{\mathrm{L}} = (\alpha_{\mathrm{CP}} + \alpha_{\mathrm{CEP}})\Delta\mu(0), \tag{2}$$

$$\Delta H_{\mathrm{L}} = -86\left(\frac{\mathrm{kG}}{\mu_{\mathrm{B}}}\right)\Delta\mu(0), \tag{3}$$

where α_{CP} and α_{CEP} are constants of proportionality between ΔH_{L} and $\Delta\mu(0)$, caused by the core polarization and conduction electron polarization mechanisms, respectively. We reference all HMF perturbations to the HMF of pure iron metal, and all changes in the individual components of the HMF perturbations (e.g., ΔH_{L} and ΔH_{NL}) are referenced to their values in pure Fe.

Each solute neighbor out to the fifth or sixth nearest-neighbor shell can alter the magnetic moment at the ^{57}Fe atom [69–72]. To accommodate environments with multi-

ple solute neighbors, we assume additivity of the changes in $\Delta\mu(0)$ from solute neighbors. (Additivity is valid for dilute solute concentrations.)

$$\Delta H_{\mathrm{L}} = -86\left(\frac{\mathrm{kG}}{\mu_{\mathrm{B}}}\right)\sum_{\boldsymbol{r}\neq 0}\delta(\boldsymbol{r})g_X^{\mathrm{Fe}}(r). \tag{4}$$

The sum is performed over the vectors, $\boldsymbol{r}$, connecting the ^{57}Fe atom to all its neighboring lattice sites. The Kroneker delta function equals 1 if the site is occupied by a solute atom, and equals 0 if it is occupied by an iron atom. The variable $g_X^Y(r)$ is the change in magnetic moment of a Y atom when it has an X solute in its coordination sphere of radius $|\boldsymbol{r}|$. (We assume that the magnetic disturbances are the same for each site in a nearest-neighbor shell.) All perturbations of iron magnetic moments are referenced to μ_{Fe}^0, the magnetic moment of an iron atom in pure iron.

The second component is a transferred HMF, H_{NL}. It arises from spin polarizations of nonlocal 4s electrons at the ^{57}Fe nucleus, caused by exchange interactions with spins at neighboring atoms. For a solute atom at $\boldsymbol{r}$ having a magnetic moment, $\mu(\boldsymbol{r})$, differing from $\mu_{\mathrm{Fe}}^0(\boldsymbol{r})$, the change in H_{NL} is:

$$\Delta H_{\mathrm{NL}} = \alpha_{\mathrm{CEP}}\sum_{\boldsymbol{r}\neq 0} f(\boldsymbol{r})\big[\mu(\boldsymbol{r}) - \mu_{\mathrm{Fe}}^0(\boldsymbol{r})\big], \tag{5}$$

where $f(\boldsymbol{r})$ is the fraction of conduction electron polarization at the ^{57}Fe nucleus produced by a change in magnetic moment at $|\boldsymbol{r}|$, with respect to the conduction electron polarization produced by the same change in magnetic moment at $|\boldsymbol{r}| = 0$.

We separate ΔH_{NL} into two terms. The direct non-local term, ΔH_{DNL}, comprises the contributions from those lattice sites occupied by solute atoms. The indirect non-local term, ΔH_{INL}, comprises the contributions from those lattice sites occupied by iron atoms, but whose magnetic moments are perturbed by nearby solute atoms:

$$\Delta H_{\mathrm{NL}} = \Delta H_{\mathrm{DNL}} + \Delta_{\mathrm{INL}}, \tag{6}$$

$$\Delta H_{\mathrm{DNL}} = \alpha_{\mathrm{CEP}}\sum_{\boldsymbol{r}\neq 0}\delta(\boldsymbol{r})f(\boldsymbol{r})\left[\left(\mu_X^0(\boldsymbol{r}) + \sum_{\boldsymbol{r}\neq\boldsymbol{r}'}\delta(\boldsymbol{r}')g_X^X\big(|\boldsymbol{r}'-\boldsymbol{r}|\big)\right) - \mu_{\mathrm{Fe}}^0\right], \tag{7}$$

$$\Delta H_{\mathrm{INL}} = \alpha_{\mathrm{CEP}}\sum_{\boldsymbol{r}\neq 0}\big(1-\delta(\boldsymbol{r})\big)f(\boldsymbol{r})\sum_{\boldsymbol{r}\neq\boldsymbol{r}'}\delta(\boldsymbol{r}')g_X^{\mathrm{Fe}}\big(|\boldsymbol{r}'-\boldsymbol{r}|\big). \tag{8}$$

All perturbations of solute magnetic moments are referenced to the magnetic moment of an isolated solute atom in an iron matrix, μ_X^0.

A homogeneous, random solid solution of Cu in bcc Fe was assumed. Input parameters to the model were obtained from neutron diffuse magnetic scattering data [73], and included the magnetic moments of Fe and Cu atoms (Fe atoms: 2.22 μ_{B} and environment-dependent; Cu atoms: 0.3 μ_{B} and constant), and the local perturbations of the magnetic moments at Fe atoms owing to nearby Cu atoms. These magnetic perturbations were assumed to have the same spatial distribution as for Ni atoms [70,71,74], but 15% of the strength. With these parameters, the calculated saturation magnetization

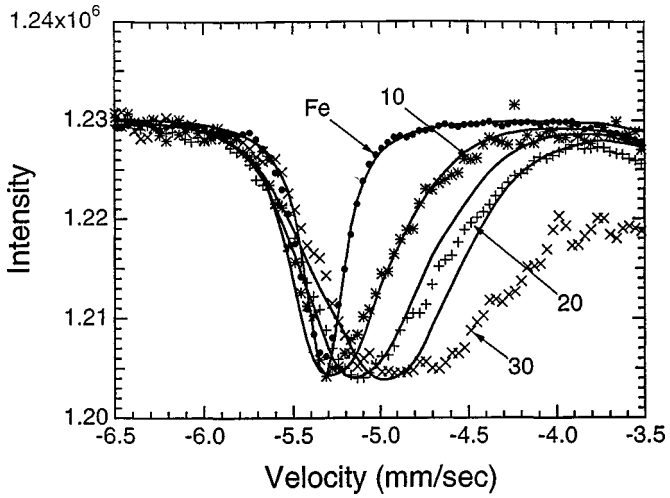

Figure 8. First peak in Mössbauer sextet from as-milled Fe–Cu alloys of different compositions (labels are in atomic % Cu). Solid curves were calculated as described in the text.

of the alloy decreased with Cu concentration somewhat slower than predicted by simple dilution. Using the definition of Kneller [75], $\beta \equiv (1/\mu_{\mathrm{Fe}})(\mathrm{d}\mu_{\mathrm{S}}/\mathrm{d}c)$, we calculated that $\beta = -0.75$ for alloys with compositions ranging from pure Fe to Fe–20% Cu. This is in reasonable agreement with magnetization data from Fe-rich alloys [75–77]. Using a pure Fe spectrum for reference, the calculated HMF distributions were converted into a sextet of peaks and convolved with a lorentzian function characteristic of our spectrometer, and these calculated spectra are presented in figure 8.

Experimental Mössbauer peaks are also presented in figure 8. With increasing Cu concentration, the peaks are shifted towards smaller velocities, and are broadened on their low-velocity sides. The same trend is found for the calculated peaks, which agree well with the experimental peaks for Fe–10% Cu, Fe–15% Cu, and Fe–20% Cu alloys. The agreement is less good for the Fe–30% Cu alloy, in part because the Fe–30% Cu spectrum contains a substantial contribution from a ferromagnetic fcc phase. Nevertheless, the spectrum from Fe–30% Cu does show that this alloy has considerably more than 20% Cu in its bcc phase. We calculated the Mössbauer spectra for other parameterizations of magnetic moments and magnetic moment perturbations in Fe–Cu alloys. For example, we had similar success in calculating the Mössbauer spectra with an alternative choice of magnetic moment for the Cu atoms, 0.1 μ_{B}, together with a somewhat larger perturbation in the magnetic moments at Fe atoms (20% of the strength of the Ni perturbations).

The spectra of figure 8 are reasonably consistent with a random solid solution of Cu in bcc Fe, owing to the good agreement between the measured Mössbauer spectra and the spectra calculated with the assumption of a homogeneous random alloy. We can therefore convert the changes in width of the Mössbauer peaks upon annealing to changes in Cu concentrations of the bcc phase. The results are presented in figure 9.

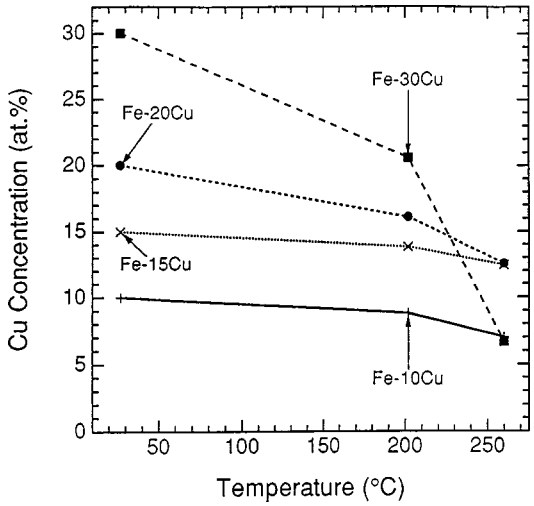

Figure 9. Cu concentration in bcc phase obtained from the changes in Mössbauer peak shapes after annealing for 0.75 h. The Fe–30 at.% Cu alloy, the only alloy containing a significant amount of fcc phase, was especially unstable against Cu segregation from the bcc phase.

There are measurable reductions in Cu concentration of the bcc phase for all alloys after annealing for 45 minutes at 200 or 260°C, but the change is especially strong for the Fe–30% Cu alloy, which was shown by X-ray diffractometry to be a two-phase mixture of fcc and bcc crystallites. We found that the reductions in the Cu concentration of the alloys Fe–10% Cu, Fe–15% Cu, and Fe–20% Cu occur without the formation of any fcc phase in the material (as measured by X-ray diffractometry).

Grain sizes of the bcc phase in Fe–Cu alloys increased after annealing. There was no systematic change of grain growth with Cu concentration in the bcc phase. In the bcc Fe–Cu alloys, the loss of Cu from the bcc phase measured by Mössbauer spectrometry could have occurred by the segregation of Cu atoms to grain boundaries, but also by the alternative process of forming Guinier–Preston (G.P.) zones. The latter possibility seems less likely from Mössbauer spectrometry work, however, since such Cu-rich zones should cause some Fe atoms to be found in a weakly magnetic, Cu-rich environment. No components with low HMFs were found in the Mössbauer spectra.

Nevertheless, these results showing minimal suppression of grain growth by Cu segregation suggested the possibility that the Cu segregation was not necessarily to grain boundaries, but rather to Cu-rich heterogeneities within the bcc crystallites. To help resolve this ambiguity, we performed small angle neutron scattering measurements on samples of ball-milled nanocrystalline samples of Fe–20 at.% Cu that were as-milled, and annealed at temperatures of 260 and 350°C. Small angle neutron scattering (SANS) is sensitive to heterogeneities in the neutron scattering density of the material. Specifically, SANS provides the Fourier transform of the density–density correlation function of the coherent neutron scattering from the material. The SANS intensity is a function

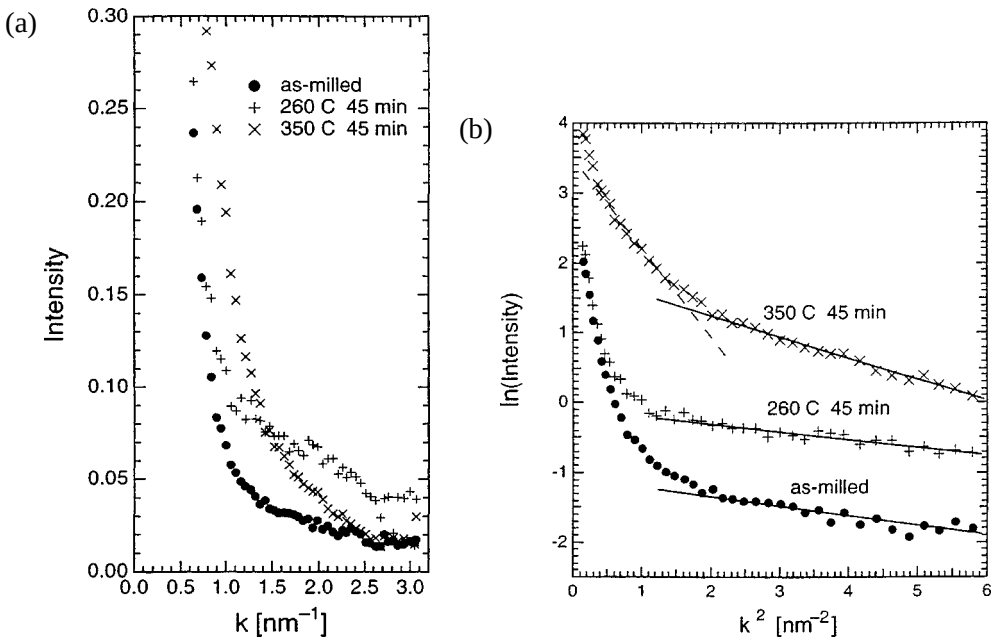

Figure 10. (a) Nuclear SANS intensity (obtained for a direction parallel to the magnetic field applied to the sample) from Fe–20 at.%Cu as-milled and after annealing at 260°C for 45 min. (b) Guinier plot of nuclear scattering from Fe–20 at.%Cu as-milled and after annealing at 260 and 350°C for 45 min. Curves were offset vertically for clarity.

of scattering vector, **Q**, and the fractional variations in the nuclear density, $\Delta\rho(x)$, as:

$$I(Q) \propto |b_{\mathrm{Fe}} - b_{\mathrm{Cu}}|^2 \left| \int_{-\infty}^{\infty} \mathrm{e}^{\mathrm{i}Qx} \left[\int_{-\infty}^{\infty} \Delta\rho(x')\Delta\rho(x+x')\,\mathrm{d}x' \right] \mathrm{d}x \right|^2, \tag{9}$$

where b_{Fe} and b_{Cu} are the coherent scattering lengths for natural isotopic distributions of Fe and Cu nuclei. By applying a strong magnetic field to saturate the magnetization of the sample, the scattering from magnetic heterogeneities can also be measured. In this case the prefactor of eq. (9) is proportional to $|\mu_{\mathrm{Fe}} - \mu_{\mathrm{Cu}}|^2$.

Figure 10(a) presents the nuclear SANS data from the as-milled material, and the material after annealing at 260°C. There is a significant increase in intensity at large Q, consistent with an increase in chemical heterogeneities in the material. Since a Q of 2 nm^{-1} corresponds to about 3 nm in real space, these heterogeneities are quite small – comparable to the grain boundary width reported in section 3.

A more quantitative analysis of the spatial correlation length is possible with a Guinier analysis [78], using a graph as in figure 10(b). The straight-line fit to the as-milled data provides a Guinier radius of gyration of 0.6 nm, which is indeed comparable to the correlation length of grain boundaries in the nanocrystalline materials. It is certainly too small to be the scale of an early stage of chemical unmixing such as spinodal decomposition. The Guinier radius is not much affected by the annealing at 260°C, al-

though the scattering at large Q becomes more intense, indicative of a stronger compositional heterogeneity. After annealing 350°C, however, the Guinier radius increases about 40%. These SANS results are consistent with the segregation of Cu to grain boundaries. The data of figure 10(a) and (b) show that during the annealing at 260°C, the grain boundaries became enriched in Cu, but remained about the same thickness. The annealing at 350°C caused the Cu segregation to the grain boundaries to extend over a larger spatial distance.

It is interesting to compare results from these two studies on nanocrystalline materials prepared by high energy ball milling: the addition of 5% Nb to Fe_3Si, and the addition of up to 20% Cu to bcc Fe. In both cases, microstructural characterizations by Mössbauer spectrometry and other techniques showed that the Nb or Cu solutes segregated to the grain boundaries upon thermal annealing. The grain boundaries in bcc Fe–Cu showed a significant capacity for absorbing Cu atoms, but this had little effect on grain growth tendencies. With further Cu segregation, the grain boundaries increase in thickness, or at least the zone of Cu segregation becomes wider. It is evidently incorrect to assume a constant areal density of sites for solute segregation to a grain boundary.

Grain size measurements showed that grain growth was suppressed significantly by the addition of Nb to the Fe_3Si. The segregation of Nb to grain boundaries also correlated to the development of $D0_3$ chemical order in the alloy, however, so we must be cautious in claiming a causal relationship. Nevertheless, assuming that the grain boundary segregation of Nb was the cause of the suppressed grain growth, it is interesting to compare the cases of Nb and Cu segregation. Although the heat of mixing in bcc Fe is even more positive for Cu than Nb, suppression of grain growth was ineffective for Cu segregants. This may indicate that the strategy for suppression of grain growth by grain boundary segregation depends less on the thermodynamic heat of mixing, and more on metallic radius or perhaps the diffusional kinetics of atom movements, which are expected to be slower for Nb than for Cu segregants.

5. Grain boundary internal structure

5.1. Grain boundary atomic structure

Previous experiments on nanocrystalline materials have indicated that their grain boundaries may differ from those of conventional polycrystalline materials [1–5,39,40]. We found possible evidence for the importance of grain boundary structure in a study of phonons in nanocrystalline Ni_3Fe. As-milled nanocrystalline Ni_3Fe has a phonon density of states that is smeared out in comparison to the DOS of large-grained material. Annealing at low temperatures, or even a quench to 10 K, then causes the phonon spectrum to sharpen considerably [79]. We followed this work on phonons by a study of grain boundary structure using small angle neutron scattering, SANS, and Mössbauer spectroscopy to examine atomic magnetic moment and structural changes in the grain boundaries after low temperature-treatments [45,80]. In this section we report results from measurements on nanocrystalline Ni_3Fe in the as-milled state, after annealing at

the low temperatures of 100°C and 265°C, and after exposure to a cryogenic temperature of 10 K [45,80]. These low temperature heat treatments caused no change in the grain size. The 4 K exposure and annealing at 100°C did not even affect the internal stress as measured by X-ray diffractometry. We used Mössbauer spectrometry and SANS to identify internal changes in the grain boundary structure.

The SANS measurements were performed over a Q range of 0.002504–2.059 nm^{-1}. The data at large Q were particularly important for obtaining information about the atomic density distribution inside the grain boundaries. The samples were saturated magnetically to allow for the separation of nuclear and magnetic scattering profiles. Trends in the grain boundary structure are seen most easily by converting the nuclear and magnetic scattering profiles into radial distribution functions (RDF), $G(R)$, by Fourier transformation of the scattering intensity, $I(Q)$:

$$G(R) = \frac{1}{2\pi^2 R} \int_{Q_{\min}}^{Q_{\max}} Q \, \sin(QR) \, I(Q) \, \mathrm{d}Q. \tag{10}$$

After the nuclear and magnetic scattering profiles were converted into RDF's, the scattering intensity from the control sample was subtracted. The resulting RDF's should originate primarily with features of the nanocrystalline structure, and not the structure of the larger powder particles and their internal cracks, which were approximately the same for all materials. (There is some possibility that features of the powder size may be correlated to nanocrystalline features, but we expect this to be a secondary effect.) Some results are shown in figure 11.

The RDF's of the magnetic scattering show a decrease after both thermal treatments. (This is consistent with an increase in grain boundary magnetic moments as observed in the SANS study of the 265°C annealed sample, which is discussed in more detail below.) There is a larger decrease in the magnetic RDF of the sample exposed to 4 K, indicating that it probably has grain boundaries with a higher average magnetic moment than the sample annealed at 100°C. The RDF's of the nuclear scattering show different changes after the thermal treatments. The RDF of the sample annealed at 100°C shows a decrease over all R. The RDF of the sample exposed to 4 K shows an increase at small R and then a decrease as R becomes larger. The differences in the shapes of the curves at small R are an indication that there are different grain boundary density distributions for the three materials. Specifically, it appears that the low temperature thermal treatments cause a larger gradient in atomic density between the crystallites and the grain boundaries. From the slope of the log–log curves of the nuclear and magnetic scattering profiles, similar information can be obtained about the structural changes induced by thermal treatment [80]. For scattering from isolated particles of the same size and shape, a slope of -4 is expected at large Q. This slope is not observed for our samples, however, because of the distribution of crystal sizes and shapes. Previous mathematical modeling [81–83] has shown that the continuity of density change at the boundary of a scatterer will affect the slope of the log–log curves. The intensity profile from a scatterer with a discontinuous or abrupt boundary has a smaller slope than the intensity from a scatterer with a continuous change in density at its boundary. A decrease in slope could

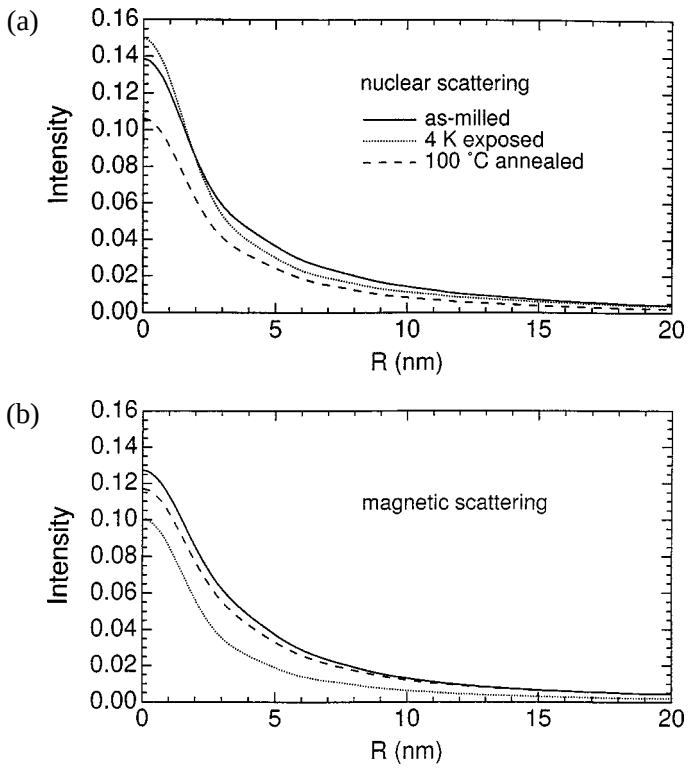

Figure 11. The (a) nuclear and (b) magnetic scattering radial distribution functions of 6nm as-milled powder, the powder after exposure to 4 K, and the powder after annealing at 100°C. The scattering intensity of the control sample has been subtracted.

indicate an increase in the density gradient at the grain boundary. The nuclear scattering log–log curves over the region of 0.5 to 2.059 nm^{-1} have slopes of -2.75, -2.7, and -2.37 for the as-milled sample, the sample annealed at 100°C, and the sample exposed to 4 K [80]. The sample exposed to 4 K appears to have the largest density gradient between its crystalline and grain boundary regions.

Mössbauer spectrometry provided further evidence for atomic rearrangements within the grain boundaries of nanocrystalline Ni_3Fe subjected to low temperature thermal treatments. The spectra in the middle of figure 12(b) are difference spectra, obtained by subtracting the as-milled spectrum from each spectrum of the thermally-treated material. The larger intensity in the difference spectrum of the material annealed at 100°C is consistent with the larger changes in the nuclear SANS seen in figure 11(a). The sample annealed at 100°C has difference peaks at ± 5.2 mm/s. In working with normalized spectra, a loss of spectral intensity at small velocities (-1.5 to $+1.5$ mm/s) must be compensated by a gain of intensity in another part of the velocity range. For the material annealed at 100°C, this seems to be primarily at the velocities of the sextet arising from the crystalline material. In other words, the loss of atoms with the most perturbed hyperfine magnetic field (-1.5 to $+1.5$ mm/s), which probably represents the most disordered

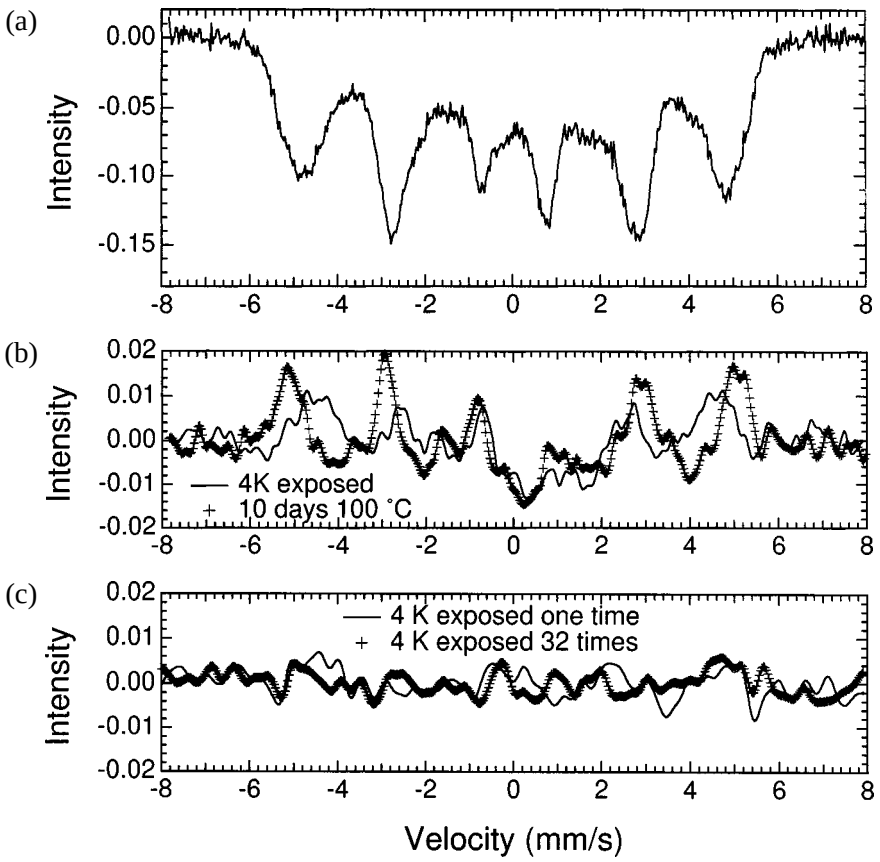

Figure 12. (a) Mössbauer spectrum of Ni_3Fe, milled 24 h with 20 : 1 ball-powder weight ratio. (b) The differences between the Mössbauer spectra of thermally-treated samples and the as-milled samples. Samples were immersed in liquid helium for approximately 20 min. (c) The differences between the Mössbauer spectra of samples exposed to 4 K and the as-milled samples. Samples were immersed in liquid helium between 1 and 32 times. This batch of nanocrystalline material did not undergo so large a change in the Mössbauer spectra during cryogenic exposure as did the material of part (b).

grain boundary regions, is compensated by a gain of atoms in the crystalline regions. The differential spectrum for the material exposed to 4 K does not show a transfer of intensity directly into the main sextet, but the intensity seems to be enhanced at the intermediate velocities around ± 4.5 mm/s that are associated with disordered environments. It seems that cryogenic exposure and low temperature annealing cause different types of changes in the grain boundary component of the Mössbauer spectra.

Mössbauer spectra were also obtained from samples exposed to 4 K from 1 to 32 times by immersion in liquid helium. The resulting difference spectra between the as-milled and the 4 K exposed samples showed little change compared to the sample exposed one time (figure 12(c)). Most of the structural change resulting from the 4 K treatment occurs during the first cryogenic exposure. Further cryogenic exposures, or

additional time at 4 K, caused only limited structural changes of the grain boundary atoms.

In summary, both Mössbauer spectrometry and SANS indicate differences in the grain boundary density when the as-milled nanocrystalline Ni_3Fe is exposed to 4 K or annealed at the low temperature of 100°C. Furthermore, it appears that the two types of thermal treatment cause different types of density distributions within the grain boundaries. The exposure to 4 K causes a larger density gradient between the crystalline and grain boundary regions. The difference in the types of internal grain boundary relaxations presumably originates with differences in the types of atom movements induced by low temperature annealing and by cryogenic exposure. The movements of grain boundary atoms in the sample exposed to 4 K are probably induced by differential thermal contraction between the grain boundary region and the crystalline regions of material. The nanocrystals and disordered grain boundaries contract by different amounts at low temperature, leading to stresses, especially at the interfaces between the grain boundaries and the crystals. It seems that the grain boundary atoms tend to move into crystalline positions. During an annealing at 100°C, vibrational energy is delivered to all the atoms in the sample, and diffusional processes are responsible for atom movements. Presumably the atoms that move are those with lower activation barriers for a diffusive jump. These need not be the same atoms as those induced to move by the stresses of differential thermal contraction. Perhaps the atoms that move are those in the most severely distorted structural environments, but their motion need not increase the sharpness of the density difference between the crystalline and grain boundary regions.

5.2. Grain boundary magnetic structure

It is expected that few atom movements can occur during an annealing at 100°C. More atom movements are expected when Ni_3Fe is annealed at 265°C, although X-ray diffractometry and transmission electron microscopy showed negligible grain growth at this low temperature. We performed a SANS and Mössbauer spectrometry study on as-milled nanocrystalline materials with a grain size of 15 nm. Annealing at 265°C created a nanocrystalline material with a similar crystal size distribution, but with reduced internal stress.

To isolate features of the RDF associated with the nanocrystals themselves, the SANS intensity profile, $I(Q)$, for a control sample of large-grained powder was subtracted from the $I(Q)$ for the as-milled material and from the $I(Q)$ of the material annealed at 265°C. The differences were converted into the RDF's shown in figure 13.

The salient feature of figure 13 is that the RDF's for the nuclear scattering are approximately similar, but those for the magnetic scattering are quite different. Some small changes in grain boundary atomic density may have occurred after annealing. The larger change of the magnetic RDF, however, is associated with changes in the grain boundary magnetic moments. The magnetic RDF for the samples annealed at 265°C is relatively small for small values of R. This indicates that the average magnetic moment of the

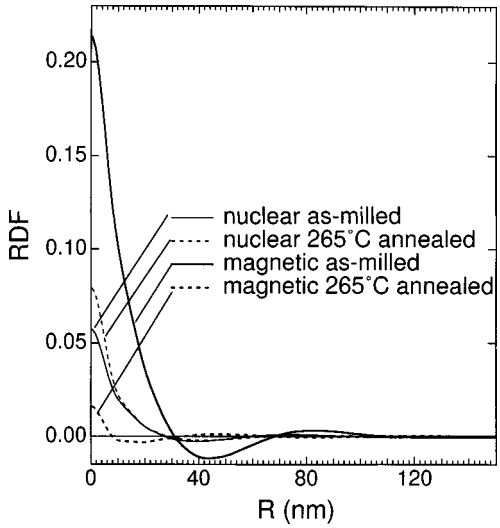

Figure 13. Radial distribution functions for the as-milled powder and powders after annealing at 265°C. Scattering for sample annealed at 600°C has been subtracted.

grain boundary is not much smaller than that of the crystalline part of the sample. The larger magnetic RDF at small R for the as-milled sample indicates that its grain boundaries have a smaller average magnetic moment, causing a greater magnetic contrast in the SANS.

Since the nuclear RDF's of the as-milled and annealed samples are similar, it can be assumed that the two samples have essentially the same atom distributions. Using this assumption, with the values of $G(0)$ for the as-milled and 265°C annealed samples we estimated a 32% change in the magnetic scattering amplitude of the grain boundary atoms after annealing. With the average magnetic moment of bulk Ni_3Fe being 1.2 μ_B/atom, we estimate that after annealing the average magnetic moments in the grain boundary increases about 0.37 μ_B/atom [45]. A similar change was obtained from the HMF distributions. The first moment of the low field component below 242 kG (see figure 1) was used to estimate the average magnetic moment of the grain boundary. This semi-quantitative estimate assumed a proportionality between magnetization and the HMF, $\mu_{GB} = \mu_{XTL} H_{GB}/287$ kG. Using the magnetic moment of crystalline Fe–Ni, $\mu_{XTL} = 1.2\ \mu_B$/atom, we obtain for the magnetic moments of the grain boundaries in as-milled material $\mu_{XTL} = 0.6\ \mu_B$/atom, and for the material annealed at 265°C, $\mu_B = 0.8\ \mu_B$/atom. We emphasize that these values are probably lower bounds for the magnetic moments of grain boundary atoms. The Ni magnetic moments are probably less affected by structural disorder than are magnetic moments at ^{57}Fe atoms, since the 3d↑ states at Ni atoms are filled. The increase in magnetization of the grain boundary after annealing at 265°C is, however, adequately consistent with the results from magnetic SANS.

6. Conclusions

In combination with other experimental techniques, Mössbauer spectrometry is a simple and powerful tool for studying structural, chemical, and magnetic features of grain boundaries in nanocrystalline materials. For materials with grain sizes below 10 nm, the large number of atoms at grain boundary sites often permits the identification and isolation of a distinct component in the Mössbauer spectrum from atoms situated at and near grain boundaries. The fraction of these atoms can be determined from the fractional amount of grain boundary component in the spectrum, and the width of the grain boundaries can be estimated with additional information about the grain size. We found a characteristic grain boundary width of 0.5 nm for fcc alloys, and a bit more than 1 nm for bcc alloys. These narrow widths of grain boundaries rule out the possibility that "gas-like" atom arrangements exist within the grain boundaries of these nanocrystalline materials.

Mössbauer spectrometry can be used to determine chemical compositions over dimensions as small as the first-nearest neighbor shell of ^{57}Fe atoms in bcc Fe alloys. (This is perhaps the smallest spatial scale over which a local composition can be defined.) Mössbauer spectrometry can therefore be used for measuring the loss of solute atoms from crystalline regions during solute segregation to grain boundaries. In this way, Mössbauer spectrometry was used for identifying the effects of Nb and Cu segregation on the grain growth tendencies of Fe_3Si–Nb and Fe–Cu alloys. It is worth noting that for nonequilibrium Fe–Cu alloys it was not possible to prepare calibration standards, and the chemical information was based on a model of how hyperfine magnetic fields originate with local magnetic moments in bcc alloys. Nanocrystalline materials often have nonequilibrium chemical compositions, so calculations of chemical effects on Mössbauer spectra from bcc Fe-rich alloys can be an important capability.

Finally, it appears possible to use Mössbauer spectrometry for qualitative studies of atom movements within grain boundaries of nanocrystalline materials that take place during low temperature annealings or cryogenic exposures. Data on nanocrystalline Ni_3Fe from Mössbauer spectrometry and small angle neutron scattering (SANS) measurements at large Q were compared. Both methods showed internal relaxations of the atoms within grain boundaries. These atom movements tended to increase the density gradient between the crystalline and grain boundary regions, especially for materials exposed to cryogenic temperatures. At higher annealing temperatures, there was a distinct increase in the magnetic moments of the atoms within the grain boundaries.

Acknowledgements

It is a pleasure to acknowledge collaborations on the science of nanocrystalline materials with Prof. H. Ouyang, Dr. Z.-Q. Gao, Dr. L.-B. Hong, Prof. H. Kuwano, Dr. J.L. Robertson, Dr. S. Spooner, Prof. W.L. Johnson, and Dr. T.A. Stephens. This work was supported by the U.S. National Science Foundation under contract DMR-9816617.

References

[1] R. Birringer, H. Gleiter, H.-P. Klein and P. Marquardt, Phys. Lett. A 102 (1984) 365.
[2] R. Birringer, Mater. Sci. Engr. A 117 (1989) 33.
[3] H. Gleiter, Prog. Mater. Sci. 33 (1989) 223.
[4] X. Zhu, R. Birringer, U. Herr and H. Gleiter, Phys. Rev. B 35 (1987) 9085.
[5] T. Haubold, R. Birringer, B. Lengeler and H. Gleiter, Phys. Lett. A 135 (1989) 461.
[6] M.R. Fitzsimmons, J.A. Eastman, M. Mullerstach and G. Wallner, Phys. Rev. B 44 (1991) 2452.
[7] J.A. Eastman, M.R. Fitzsimmons and L.J. Thompson, Philos. Mag. B 66 (1992) 667.
[8] J. Löffler and J. Weissmüller, Phys. Rev. B 52 (1995) 7076.
[9] F. Boscherini, S. de Panfilis and J. Weissmüller, Phys. Rev. B 57 (1997) 3365.
[10] G.J. Thomas, R.W. Siegel and J.A. Eastman, Scripta Metall. Mater. 24 (1990) 201.
[11] W. Wunderlich, Y. Ishida and R. Maurer, Scripta Metall. Mater. 24 (1990) 403.
[12] R.W. Siegel, MRS Bulletin 15 (1990) 60 and cover.
[13] S.K. Ganapathi and D.A. Rigney, Scripta Metall. Mater. 24 (1990) 1675.
[14] R.W. Siegel and G.J. Thomas, Ultramicroscopy 40 (1992) 376.
[15] E.A. Stern, R.W. Siegel, M. Newville, P.G. Sanders and D. Haskel, Phys. Rev. Lett. 75 (1995) 3874.
[16] B. Fultz, G. Le Caër and P. Matteazzi, J. Mater. Res. 4 (1989) 1450.
[17] U. Herr, J. Jing, R. Birringer, U. Gonser and H. Gleiter, Appl. Phys. Lett. 50 (1987) 472.
[18] P. Sinha and G.S. Collins, Hyp. Interact. 92 (1994) 949.
[19] H. Kuwano, H. Ouyang and B. Fultz, Nanostruct. Mater. 1 (1992) 143.
[20] H. Kuwano, H. Ouyang and B. Fultz, Mater. Sci. Forum 88–90 (1992) 561.
[21] C. Michaelsen and E. Hellstern, J. Appl. Phys. 62 (1987) 117.
[22] P. Matteazzi and G. Le Caër, J. Am. Ceram. Soc. 74 (1991) 1382.
[23] G. Le Caër, P. Matteazzi and B. Fultz, J. Mater. Res. 7 (1992) 1387.
[24] T. Tanaka, S. Nasu, B. Huang, K.N. Ishihara and P.H. Shingu, Nucl. Instr. Mem. Phys. Res. B 76 (1993) 195.
[25] O. Mao, R.A. Dunlap and J.R. Dahn, J. Electrochem. Soc. 146 (1999) 405.
[26] A. Hightower, P. Delcroix, G. Le Caër, C.-K. Huang, B.V. Ratnakumar, C.C. Ahn and B. Fultz, J. Electrochem. Soc. 147 (2000) 1.
[27] S.J. Campbell and W.A. Kaczmarek, in: *Mössbauer Spectroscopy Applied to Magnetism and Materials Science*, Vol. 2, eds. G.J. Long and F. Grandjean (Plenum Press, New York, 1996) pp. 273–330.
[28] B. Fultz, H. Kuwano and H. Ouyang, J. Appl. Phys. 77 (1995) 3458.
[29] E. Hellstern, H.J. Fecht and W.L. Johnson, J. Mater. Res. 4 (1989) 1292.
[30] E. Hellstern, Z. Fu and W.L. Johnson, Adv. Powder Metall. 1–3 (1989) 111.
[31] C. Gente, M. Oehring and R. Bormann, Phys. Rev. B 48 (1993) 13 244.
[32] E. Ma and M. Atzmon, Mater. Chem. Phys. 39 (1995) 249.
[33] B. Fultz, J.L. Robertson, T.A. Stephens, L.J. Nagel and S. Spooner, J. Appl. Phys. 79 (1996) 8318.
[34] H.N. Frase, L.J. Nagel, J.L. Robertson and B. Fultz, Philos. Mag. B 75 (1997) 335.
[35] W.L. Johnson, private communication;
Y. Abe, Ph.D. thesis, Materials Science, California Institute of Technology (1993).
[36] J. Weissmüller, J. Mater. Res. 9 (1994) 4.
[37] P. Haasen, *Physical Metallurgy*, 2nd ed. (Cambridge Univ. Press, 1992) p. 370.
[38] T. Haubold et al., Phys. Lett. A 135 (1989) 461.
[39] M. Hirscher et al., Journal of Magnetism and Magnetic Materials 146 (1995) 117.
[40] R. Würschum, K. Reimann, S. Gruss, A. Kubler, P. Scharwaechter, W. Frank, O. Kruse, H.D. Carstanjen and H.E. Schaefer, Philos. Mag. B 76 (1997) 407.
[41] F.R.N. Nabarro, *Theory of Crystal Dislocations* (Dover, Mineola, NY, 1987).
[42] D. McLean, *Grain Boundaries in Metals* (Clarendon Press, Oxford, 1957).
[43] G.A. Chadwick and D.A. Smith, *Grain Boundary Structure and Properties* (Academic Press, New York, 1976).

[44] H.J. Fecht, E. Hellstern, Z. Fu and W.L. Johnson, Metall. Trans. A 21 (1990) 2333.
[45] H.N. Frase, B. Fultz, S. Spooner and J.L. Robertson, J. Appl. Phys. 85 (1999) 7097.
[46] G. LeCaër and J.M. Dubois, J. Phys. E 12 (1979) 1083.
[47] H.P. Klug and L.E. Alexander, *X-Ray Diffraction Procedures* (Wiley, New York, 1974) pp. 661–665; A.G. Khachaturyan, Sov. Phys. Cryst. 5 (1960) 335.
[48] B.E. Warren and B.L. Averbach, J. Appl. Phys. 21 (1950) 595.
[49] B.E. Warren, *X-Ray Diffraction* (Dover, Mineola, NY, 1990) pp. 257–274.
[50] C.N.J. Wagner and M.S. Boldrick, Mater. Sci. Eng. A 133 (1991) 26.
[51] J. Hesse, Hyp. Interact. 47 (1989) 357.
[52] D.G. Rancourt and J.Y. Ping, Hyp. Interact. 69 (1991) 497.
[53] J.Y. Ping, D.G. Rancourt and R.A. Dunlap, J. Magn. Magn. Mater. 103 (1992) 285.
[54] H. Ouyang, Grain boundaries of nanophase materials, Ph.D. in Materials Science, California Institute of Technology (October 12, 1992).
[55] M. Brendel, Ph.D. thesis, Fachbereich Physik, Technologie der Universität, GH, Duisburg (1990).
[56] J.M. Pennison, R. Gronsky and J.B. Brosse, Scripta Metall. 16 (1982) 1239.
[57] G.H. Campbell, P. Gumbsch, W.E. King and M. Rühle, Z. Metallk. 83 (1992) 472.
[58] T.B. Massalski, *Binary Alloy Phase Diagrams* (ASM, Metals Park, OH, 1986).
[59] F.S. Galasso, *Structure and Properties of Inorganic Solids* (Pergamon Press, Oxford, England, 1970) pp. 8–11.
[60] Z. Gao and B. Fultz, Nanostruct. Mater. 2 (1993) 231.
[61] Z. Gao and B. Fultz, Hyp. Interact. 94 (1994) 2213.
[62] M.B. Stearns, Phys. Rev. 129 (1963) 1136.
[63] Z.Q. Gao and B. Fultz, Nanostruct. Mater. 4 (1994) 939.
[64] C. Bansal, Z.Q. Gao and B. Fultz, Nanostruct. Mater. 5 (1995) 327.
[65] B. Fultz, C.C. Ahn, S. Spooner, L.B. Hong, J. Eckert and W.L. Johnson, Metall. Mater. Trans. A 27 (1996) 2934.
[66] P.J. Schilling, J.H. He, R.C. Tittsworth and E. Ma, Acta Mater. 47 (1999) 2525.
[67] B. Fultz, in: *Mössbauer Spectroscopy Applied to Magnetism and Materials Science*, Vol. I, eds. G.J. Long and F. Grandjean (Plenum Press, New York, 1993) pp. 1–31.
[68] B. Fultz and J.W. Morris, Jr., Phys. Rev. B 34 (1986) 4480.
[69] M.F. Collins and J.B. Forsyth, Phil. Mag. 8 (1963) 401.
[70] M.F. Collins and G.G. Low, Proc. Phys. Soc. 86 (1965) 535.
[71] I.A. Campbell, Proc. Phys. Soc. 89 (1966) 71.
[72] H.R. Child and J.W. Cable, Phys. Rev. B 13 (1976) 227.
[73] F. Kajzar and G. Parette, J. Appl. Phys. 50 (1979) 1966.
[74] S. Spooner and W.E. Brundage, Scripta Met. 17 (1983) 573.
[75] E.F. Kneller, J. Appl. Phys. 35 (1964) 2210.
[76] A.T. Aldred, J. Phys. C 1 (1968) 1103.
[77] E. Ma, M. Atzmon and F. Pinkerton, J. Appl. Phys. 74 (1993) 995.
[78] A. Guinier, *X-Ray Diffraction in Crystals, Imperfect Crystals, and Amorphous Bodies* (Dover, Mineola, NY, 1994) section 10.2, p. 322.
[79] H. Frase, B. Fultz and J.L. Robertson, Phys. Rev. B 57 (1998) 898.
[80] H.N. Frase, B. Fultz, J.L. Robertson and S. Spooner, Structural relaxation within the grain boundaries of nanocrystalline Ni_3Fe, Philos. Mag. 80 (2000) 1545.
[81] W. Ruland, J. Appl. Cryst. 4 (1971) 70.
[82] P.W. Schmidt, J. Appl. Cryst. 24 (1991) 414.
[83] P.W. Schmidt, D. Avnir, D. Levy, A. Höhr, M. Steiner and A. Röll, J. Chem. Phys. 94 (1991) 1474.